AGU ADVANCING EARTH AND SPACE SCIENCES

Geophysical Research Letters

RESEARCH LETTER
10.1029/2024GL109276

Retrieving Seismic Source Characteristics Using Seismic and Infrasound Data: The 2020 M_L 4.1 Kiruna Minequake, Sweden

Antoine Turquet[1], Quentin Brissaud[1], Celso Alvizuri[1], Sven Peter Näsholm[1,2], Alexis Le Pichon[3], and Johan Kero[4]

[1]NORSAR, Kjeller, Norway, [2]Department of Informatics, University of Oslo, Oslo, Norway, [3]CEA, DAM, DIF, Bruyères-le-Châtel, France, [4]Swedish Institute of Space Physics (IRF), Kiruna, Sweden

Abstract A minequake of magnitude M_L 4.1 occurred on 18 May 2020 early in the morning at the LKAB underground iron ore mine in Kiruna, Sweden. This is the largest mining-induced earthquake in Scandinavia. It generated acoustic signals observed at three infrasound arrays at 9.3 (KRIS, Sweden), 155 (IS37, Norway), and 286 km (ARCI, Norway) distance. We perform full-waveform focal mechanism inversion based on regional seismic data and local infrasound data. These independently highlight that this event was dominated by a shallow-depth collapse in agreement with in-mine seismic station data. However, regional infrasound data cannot inform the inversion process without an accurate model of atmospheric winds and temperatures. Yet, our numerical simulations demonstrate a potential of using local and regional infrasound data to constrain an event's focal mechanism and depth.

Plain Language Summary The largest mining-induced earthquake in Scandinavia (M_L 4.1) occurred on 18 May 2020 early in the morning at the LKAB underground iron ore mine in Kiruna, Sweden. The seismic waves coupled to the atmosphere and propagated large distances as sound waves which were observed at three infrasound arrays at 9.3 (KRIS, Sweden), 155 (IS37, Norway), and 286 km (ARCI, Norway) distance. Our seismic and acoustic modeling results highlight a strong collapse event within the northern section of the mine. The modeling of acoustic and seismic waves across the Earth-atmosphere suggests that sound wave data can help when determining the location and properties of a seismic source.

Antoine Turquet and Quentin Brissaud contributed equally to this work.

Key Points:

- Seismic and acoustic records indicate a strong collapse at shallow depth of 1 ± 0.5 km for the 2020 Kiruna minequake
- Focal mechanisms and depths of shallow seismic sources can be retrieved from local infrasound records
- Inversions using regional infrasound data is possible when accurate weather models are available

Supporting Information:

Supporting Information may be found in the online version of this article.

Correspondence to:

Q. Brissaud,
quentin@norsar.no

Citation:

Turquet, A., Brissaud, Q., Alvizuri, C., Näsholm, S. P., Le Pichon, A., & Kero, J. (2024). Retrieving seismic source characteristics using seismic and infrasound data: The 2020 M_L 4.1 Kiruna minequake, Sweden. *Geophysical Research Letters*, *51*, e2024GL109276. https://doi.org/10.1029/2024GL109276

Received 15 MAR 2024
Accepted 18 APR 2024

Author Contributions:

Conceptualization: Antoine Turquet, Quentin Brissaud, Celso Alvizuri, Sven Peter Näsholm, Alexis Le Pichon, Johan Kero
Data curation: Alexis Le Pichon
Formal analysis: Quentin Brissaud, Celso Alvizuri, Sven Peter Näsholm, Alexis Le Pichon
Funding acquisition: Quentin Brissaud
Investigation: Antoine Turquet, Quentin Brissaud, Sven Peter Näsholm, Alexis Le Pichon, Johan Kero

1. Introduction

Underground seismic sources, for example, earthquakes and man-made explosions, excite seismic waves that couple to the atmosphere and propagate as infrasound – low-frequency acoustic waves below 20 Hz – over great distance (Dannemann Dugick et al., 2023; Donn & Posmentier, 1964). Recent studies highlight correlations between earthquake magnitude, ground motion, and infrasound amplitude (Hernandez et al., 2018; Mutschlecner & Whitaker, 2005; Shani-Kadmiel et al., 2018; Vallage et al., 2021). However, few studies have investigated the relationships between focal depth and focal mechanism with the acoustic wavefield (Brissaud et al., 2021; Inchin et al., 2021; Shani-Kadmiel et al., 2021; Yang et al., 2021). Shani-Kadmiel et al. (2021), as well as Inchin et al. (2021), successfully recovered the main rupture mechanism properties of large-magnitude earthquakes at low frequency. However, these inversions benefited from large earthquake magnitude and favorable downwind station locations. There is a lack of datasets that incorporate local and regional infrasound data from earthquakes (or minequakes). Therefore, it remains challenging to link earthquake rupture mechanism, subsurface velocity structure, topography, and atmospheric path effects to infrasound observations at local and regional distances.

Discriminating between source and path effects at large distances from the source is difficult as path effects (e.g., atmospheric absorption, scattering, dispersion, and refraction) can significantly influence acoustic waveforms. Since infrasound observations are typically reported at regional or global ranges, where path effects dominate (>100 km distance), the interpretation of infrasound to retrieve source physics is challenging (Shani-Kadmiel et al., 2021). Even at closer ranges (<100 km), source directivity can significantly impact the epicentral infrasound along the surface to prevent observations in shadow zones (Arrowsmith et al., 2012). Theoretical and experimental studies of surface and buried explosions have provided seismo-acoustic coupling insights. In particular, the ratio between seismic and acoustic amplitudes depends greatly on focal depth (Lai et al., 2021).

Methodology: Quentin Brissaud, Celso Alvizuri, Sven Peter Näsholm, Alexis Le Pichon
Project administration: Quentin Brissaud
Software: Quentin Brissaud, Celso Alvizuri
Supervision: Antoine Turquet, Quentin Brissaud, Sven Peter Näsholm, Alexis Le Pichon
Validation: Quentin Brissaud, Sven Peter Näsholm
Visualization: Antoine Turquet, Quentin Brissaud, Celso Alvizuri, Sven Peter Näsholm
Writing – original draft: Antoine Turquet, Quentin Brissaud, Celso Alvizuri, Sven Peter Näsholm
Writing – review & editing: Antoine Turquet, Quentin Brissaud, Celso Alvizuri, Sven Peter Näsholm, Alexis Le Pichon, Johan Kero

Only sources at depths shallower than a wavelength excite evanescent seismic body waves that couple to the atmosphere as strong spherically propagating infrasound (Godin, 2011). In recent studies, remote seismically induced infrasound observations from explosive sources have been shown to provide unique insights into seismic parameters such as source depth (Averbuch et al., 2020; Lai et al., 2021) and yield (Kim & Pasyanos, 2022). Yet, due to the lack of high-quality local and regional data, there is a need for additional rupture mechanism studies based on epicentral infrasound.

In the current study, we use infrasound and seismic waveform data (both observed and synthetic) to retrieve the source mechanism and focal depth of the 18 May 2020 minequake in Kiruna, Sweden (Figure 1a). The Kiruna event ocurred at an active mining site, and is one of the largest earthquakes to have occurred in Sweden. The mine, operated by Luossavaara-Kiirunavaara AB (LKAB), is the world's largest underground iron ore mine (Figure 1b). A recent in-mine and regional seismic analysis (Dineva et al., 2022) concluded that this minequake involved a complex series of normal faulting events in the south of the mine (line AD in Figure 1b) followed by collapse events in the north of the mine (line AC in Figure 1b). In addition to seismic waves, strong ground-motion at the epicenter also excited infrasound which was recorded at KRIS, IS37, and ARCI, at 9.3, 155, and 286 km distances, respectively (Figures 1c–1e). Such observations of acoustic signals at both local and regional distances are unprecedented.

2. Data

2.1. Hypocenter and Seismic Waveform Data

The Swedish National Seismic Network (SNSN, Lund, Schmidt, Hossein Shomali, & Roth, 2021) estimated the minequake occurred on 01:11:56.2 UTC with hypocenter at 67.83965°N, 20.20759°E, and magnitude M_L 4.1 (see Figure 1b). To estimate a moment tensor mechanism for the event, described in the following sections, we obtained waveform data from all possible open seismic stations within a 1,500 km radius which includes primarily SNSN stations followed by stations in Norway, Finland, and continental Europe.

2.2. Infrasound Observations

We analyzed infrasound arrivals recorded at the four-sensor KRIS array, near Kiruna, at the ten-sensor IS37 array in Bardufoss, Norway, as well as the eight-sensor ARCI array in Karasjok, Norway (Figure 1a). Data from the infrasound arrays are processed using the Progressive Multi-Channel Correlations (PMCC) framework (Cansi, 1995).

The infrasound data at (local) station KRIS, bandpass filtered between 0.5 and 10 Hz, show clear seismic and epicentral acoustic arrivals with a dominant frequency at 2.5 Hz (Figure 1d). The inversion of the backazimuth estimate highlights that the signals were emitted from the northern section of the Kiruna mine (Supporting Sec. S3). Due to the shallow focal depth, the conversion of evanescent seismic waves at the Earth-atmosphere interface can explain a generation and propagation of infrasound from the epicenter and along the surface (Godin, 2011). Arrivals with dominant frequency below 2.5 Hz are visible continuously a few seconds before and after the main epicentral acoustic arrival 30 s after the origin time. These signals might be due to several competing factors, including tropospheric refraction, spatially and temporally distributed rupture mechanisms, and interactions with subsurface velocity structures. The possible resonance of acoustic waves within the mine (Downey et al., 2022), similar to wave resonance within magma conduits (Lai et al., 2021), might facilitate seismo-acoustic coupling at a different location than the main epicenter.

At regional distances, IS37 and ARCI data, bandpass filtered between 0.5 and 5 Hz, feature 1–5 Hz arrivals with no significant energy below 1 Hz (Figures 1c and 1e). We observe a slight increase in apparent velocity with time (0.33–0.35 km/s) indicating the arrival of higher-altitude refractions or reflections from the lower stratosphere <30 km altitude. The combination of high-frequency arrivals (>1 Hz) and stratospheric refraction or reflection suggests a shadow-zone ducting contribution. Similar structures were previously observed in connections with small-scale, <5 km vertical wavelength, gravity wave (GW) (Chunchuzov & Kulichkov, 2019; Vorobeva et al., 2023). The slightly lower amplitudes at ARCI compared to IS37 can be explained both by greater source-receiver range and the weaker ducting due to the lower effective soundspeed ratio at ARCI because of smaller stratospheric along-track winds (Figure 1a).

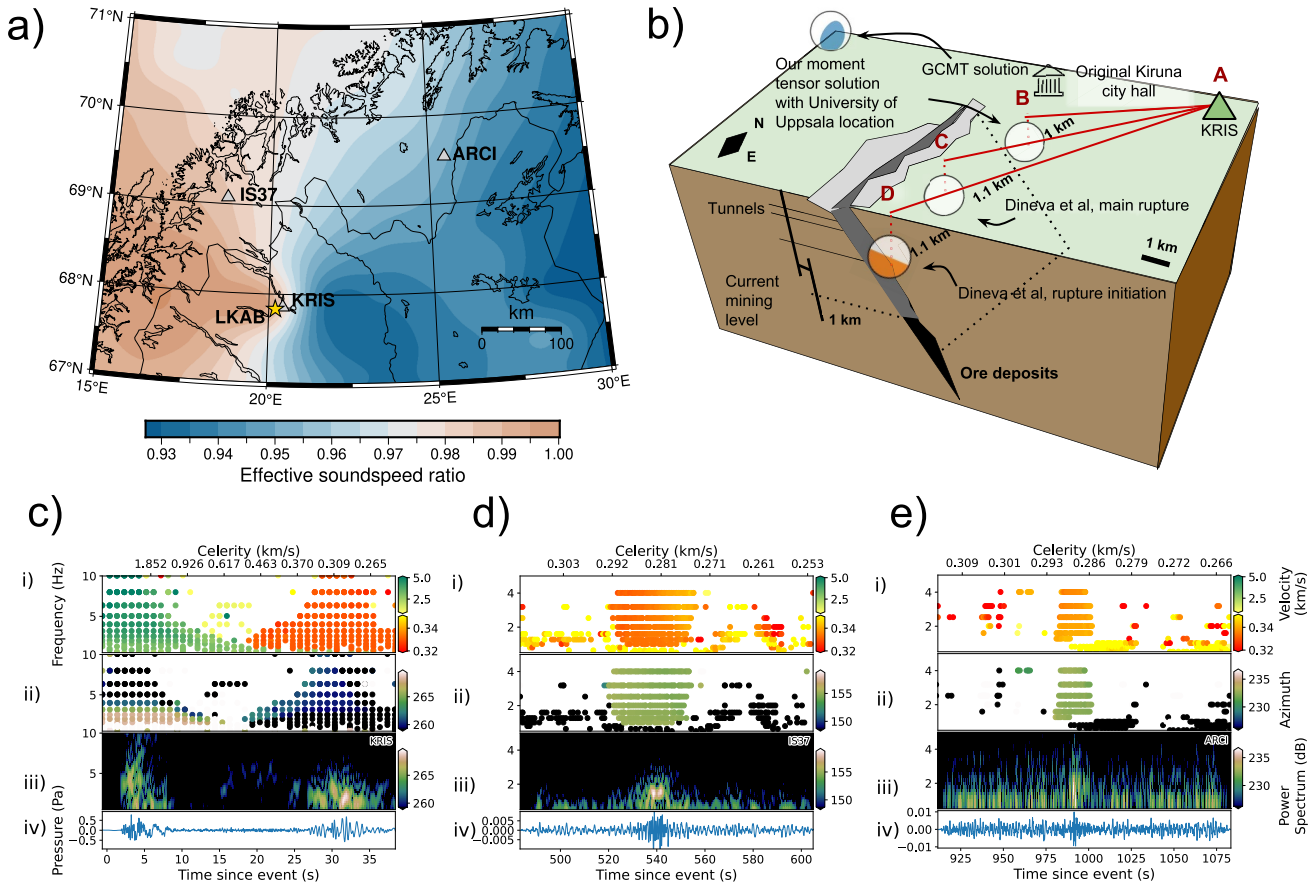

Figure 1. (a) Location of the 2020 Kiruna minequake epicenter (yellow star) and the infrasound arrays of this study (triangles). The background colors indicate the ratio between stratospheric (35–60 km altitude) and ground-level effective soundspeeds extracted from the ERA5 reanalysis model product (Hersbach et al., 2017, 2020). (b) 3D mine sketch and the KRIS array location (label A), our moment tensor solution (label B), and locations of main source types from (Dineva et al., 2022) (labels C and D) (c,d,e) PMCC processing output for KRIS, IS37, and ARCI showing, from top to bottom, the apparent velocity, backazimuth, energy, and beamformed pressure versus time and frequency.

3. Seismic Moment Tensor Estimation

We estimated seismic moment tensors and their uncertainties for the Kiruna event using the methodology of Alvizuri et al. (2018). The methodology includes processing the waveform data from all possible 3-component stations, correcting for instrument response and rotating into source-receiver frames, and removing stations with low signal-to-noise ratios or low overall quality, which resulted in a total number of stations to 93 used in our final result. In our estimate we used Rayleigh and Love waveforms bandpass filtered between 0.05 and 0.2 Hz.

The methodology performs a grid-search in moment-tensor space and involves the following steps: (a) compute synthetic seismograms for each mechanism, (b) calculate the misfit between observed and synthetic seismograms, and (c) evaluate each mechanism by its misfit and find the mechanisms with the smallest misfit. The synthetic seismograms were computed using a 1D velocity model from CRUST1.0 (Laske et al., 2013) (Supporting Sec. S7) and trapezoidal source-time function with half duration of 0.5 s. The moment-tensor uncertainties were computed from the ensemble solutions appraised during the grid search. To be comparable with other results, we did not invert for the source location nor origin time and instead used the hypocenter described in Section 2.2.

We analyzed the moment tensor results in terms of their so-called source-types and on a lune diagram (Tape & Tape, 2012). The lune organizes moment tensors by source-types, with positive isotropic (+ISO) solutions on top of the lune (usually related to explosion mechanisms), negative isotropic (–ISO) at the bottom (e.g., implosion or collapse), and double-couple at the center (e.g., tectonic earthquakes). The results for Kiruna show a best-fit mechanism with primarily negative isotropic source parameters (Figure 2 and Supporting Sec. S8). Figure 2b

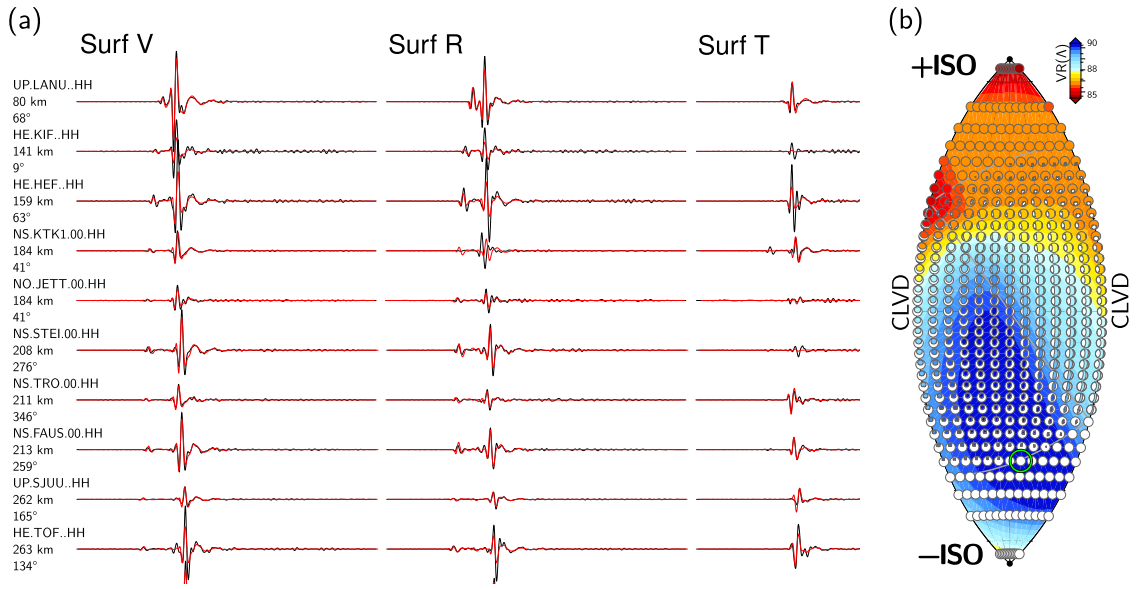

Figure 2. Moment tensor estimation results. (a) Comparison between recorded (black) and synthetic (red) seismic waveforms for the 10 closest stations out of 93 stations (see Supporting Sec. S8). (b) Full grid search summary on a lune diagram, showing the best-fitting solution at each grid point on the lune and colored by waveform fit, with best-fitting solutions in blue and worst-fitting solutions in red.

summarizes the grid search results on the lune. As shown in the figure, the best-fitting solutions are concentrated in the –ISO area while the worst-fitting solutions are toward + ISO. The corresponding seismograms for the best-fitting solution show good agreement between observations and synthetics. A recent study of collapses at various mining sites, including at Kiruna, also resolved a collapse mechanism for the event (Pasyanos et al., 2023). And though their solution and ours are similar (both show –ISO parameters) they are not identical, likely due to the different methodologies and datasets used (e.g., their analysis used 15 stations to resolve the mechanism, whereas ours used 93 stations).

4. Local Seismo-Acoustic Data Inversion

Local pressure recordings of epicentral and Rayleigh-wave infrasound (Figure 3a) can provide an independent assessment of the focal depth and source mechanism (Lai et al., 2021). We perform a full-waveform inversion of local data to retrieve the vertical and radial moment tensor components, source-station distance, origin time, while accounting for acoustic velocity uncertainties (Hejrani et al. (2017), Supporting Sec. S5). We sample the parameter space using a Markov chain Monte Carlo (MCMC) sampler with stretch moves, implemented in the emcee package (Foreman-Mackey et al., 2013a), together with Gaussian prior uncertainties in terms of origin time (±0.2 s), acoustic velocity (±8 m/s), and distance from the source (±2 km). These uncertainty values are extracted from SNSN catalog (SNSN, Lund, Schmidt, Hossein Shomali, & Roth, 2021) and ERA5 model variations in the lower troposphere (Hersbach et al., 2020). To ensure that both seismic and acoustic arrivals are contributing equally to the misfit we weigh the misfit of the acoustic arrival by a factor 2.5, that is, ratio of maximum seismic to acoustic amplitudes.

We simulate waveforms in a coupled Earth-atmosphere system using SPECFEM2D-DG (Brissaud et al., 2017; Martire et al., 2022a). This modeling tool simulates both seismic and acoustic wave propagation from a moment-tensor point source. We selected a computational domain of size 34.5 × 20 km with PML boundary conditions, used a spatial step 0.25 km, time step $5e^{-3}$ s, and applied a Gaussian source-time function with unit integral and half duration 2 s which corresponds to a smoothed boxcar function as used in Section 3. Because we performed 2D instead of 3D simulations, we first projected the full moment tensor along the azimuth between the epicenter and our receiver (Brissaud et al., 2021). The rotated moment tensor is then decomposed in three unknowns M_{xx}, M_{zz}, M_{xz} where x and z correspond to the radial and vertical components (Hu et al., 2023). We corrected for spherical geometrical spreading considering a linear propagating path (Miksat et al. (2008), Supporting Sec. S4).

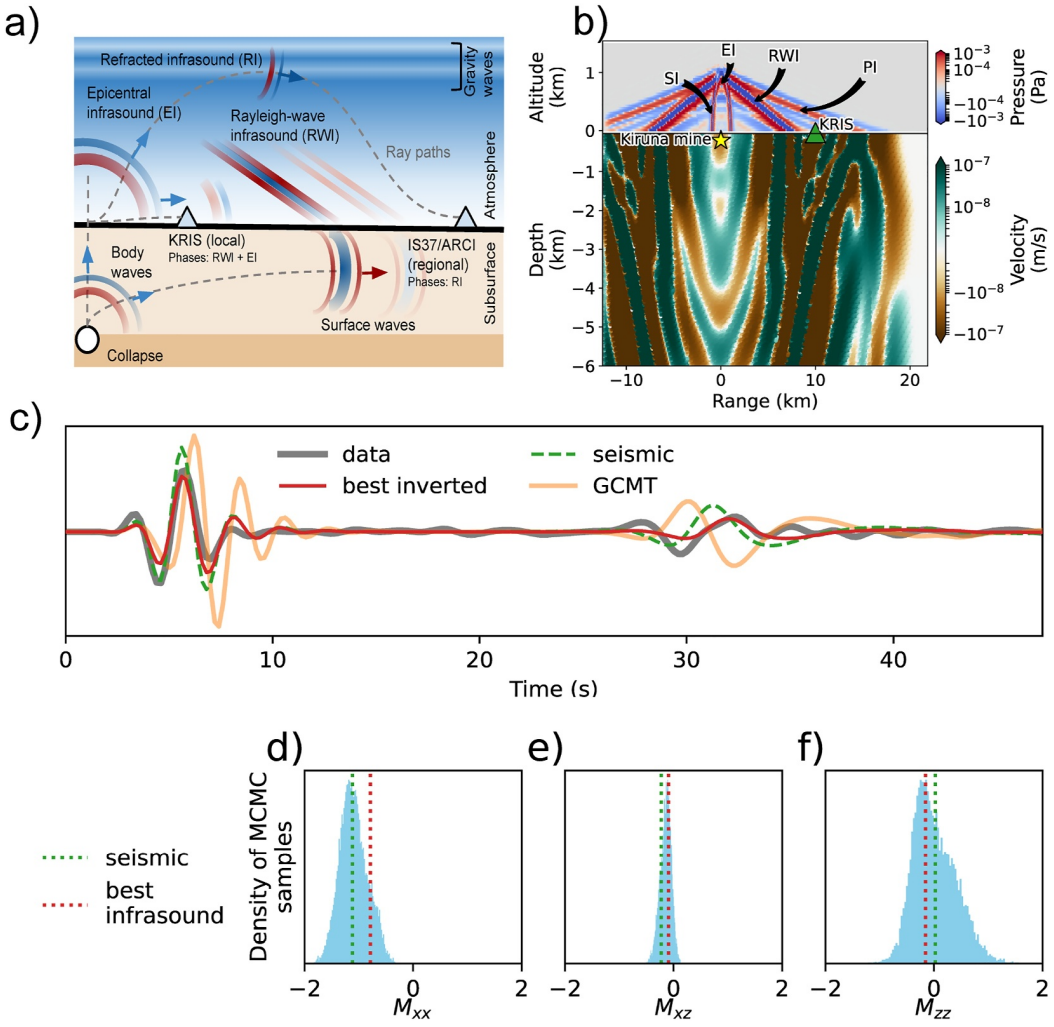

Figure 3. Local full-waveform modeling and inversion. (a) Schematic depicting seismic and infrasound propagation at local and regional distances. (b) Seismo-acoustic wavefield snapshot generated from a shallow collapse event with Epicentral Infrasound (EI), Spherical Infrasound (SI), Rayleigh Wave Infrasound (RWI), and P-wave Infrasound (PI). (c) Recorded (thick gray), and simulated waveforms, bandpass filtered between 0.05 and 0.5 Hz, with our best seismic (green) and infrasound (red) moment tensor solution as well as for the GCMT moment-tensor solution (orange) (d)–(f) Distributions of MCMC samples of 2D moment tensor components along the source-receiver axis. Vertical lines in panels (d)–(f) correspond to the infrasound solution with the lowest misfit (green) and the solution computed from regional seismic data (Section 3).

Atmospheric parameters are extracted from the ERA5 reanalysis model product (Hersbach et al., 2017, 2020), extracted at the epicenter.

The sketch of the theoretical seismo-acoustic phases both on a local and regional scale is provided in (Figure 3a) (Le Pichon et al., 2010). The simulated acoustic wavefield (Figure 3b) for a shallow collapse event at 0.5 km depth (Section 3) indicates the presence of four major seismic-to-acoustic phase arrivals: (a) low-amplitude planar wavefronts generated by scattered P waves (PI); (b) planar wavefronts due to Rayleigh waves (RWI); (c) spherical wavefronts excited by evanescent body waves (SI); (d) upward propagating wavefronts excited by direct body waves followed by upward propagating signal produced by body-wave reflections on the shallowest velocity layer (EI).

The infrasound-based solution provides a better fit to the data than the seismic-based solution (green line, Figure 3c) or with the Global Centroid Moment Tensor (GCMT, orange line, Figure 3c), which does not capture the observed seismic-to-acoustic ratio and phase owing to the lack of isotropic component. The best infrasound-based focal mechanisms corresponds to a collapse-dominated moment tensor solution similar to the original

seismic solution with variations only up to ∼10% along the radial component M_{xx} (Figure 3g). The resulting MCMC sample distribution for focal depth is bi-modal (Figure 3j) which suggests that there is a trade-off between focal depth and the accuracy of acoustic or seismic arrival predictions. Shallow sources (∼1 km) lead to a better fit of the acoustic arrival, while, conversely, deeper depths (∼2 km) produce more accurate seismic predictions (Supporting Sec. S5). This trade-off can be explained by the fact that shallow sources always produce strong acoustic arrivals which can lead to large errors if they are out-of-phase with the data. Conversely, deep sources only produce small-amplitude acoustic waves which leads to smaller errors on average across the parameter space.

Our numerical results are in agreement with the in-mine seismic inversions and analyses by Dineva et al. (2022) which highlight that the largest magnitude events occurred north of the mine as collapse events at about 1 km depth (labels C and B in Figure 1b). Additionally, Dineva et al. (2022) showed that the minequake was initiated in the southern section of the mine with normal-fault events at ∼1 km depth. To assess whether the observed arrival times and phases correspond to events in the northern or southern section of the mine, we simulated a collapse event ∼3 km south of our initial solution at 0.5 km depth (Supporting Sec. S6). The results show that the acoustic signal emitted south of the mine, compared to our initial epicentral location, has a significant delay and does not fit the observed arrivals. This suggests that the observed arrivals originate from the northern section of the mine.

Yet, the modeling is unable to capture accurately the amplitude of each phase of the acoustic arrival. This discrepancy owes to several factors, including competing effects between temporal and spatial slip distribution at shallow depths (Vallage et al., 2021), mine geometry (Downey et al., 2022), and unresolved subsurface velocity structures (Martire et al., 2018). In the case of the Le Teil earthquake, the significant near-surface vertical slip was likely the dominant infrasound source (Vallage et al., 2021). For the Kiruna minequake, Dineva et al. (2022) mentioned the possibility of surface landslides. Tunnel resonance exciting acoustic waves might also contribute to the discrepancies observed at KRIS (Downey et al., 2022).

5. Regional Infrasound Propagation Modeling

In the acoustic shadow-zone (∼50–150 km distance from the source), the presence of small-scale GWs can refract infrasound energy back to the surface (Chunchuzov & Kulichkov, 2019, Figure 3a). However, it remains unclear whether such phases contain accurate information about the source mechanism. To investigate the relationships between the source mechanism and local propagation, we model signals using, as source-time function, local recordings at KRIS corrected for geometric spreading (Averbuch et al., 2022). This assumption also means that topography and source directivity effects (focal depth and mechanism) are insignificant. These assumptions are supported by two observations: (a) High-frequency signals (>1 Hz) at KRIS, IS37, and ARCI were most likely excited by events close to the surface, which emit more energy along the surface compared to the main seismic event; (b) The low-frequency energy at KRIS (<0.5 Hz) is dominated by a collapse component, which is primarily isotropic.

Similar to Arrowsmith et al. (2012), we then model regional infrasound by considering that the source can be represented by a surface point-source at the epicenter. This enables us to simulate propagation into the far-field between 0.5 and 5 Hz using the broadband normal-mode numerical simulator ModBB (Waxler et al., 2021). This scenario would be overly computationally expensive using Galerkin full-waveform simulators such as SPECFEM-DG. The simulations were run at a frequency step $\Delta f = 2 \times 10^{-3}$ Hz. The atmospheric profiles used for these simulations are range-independent and were built from ERA5 reanalysis models extracted at the epicenter together with six GW realizations using Gardner model (see Supporting Sec. S2 and Gardner et al., 1993). The range-independent assumption is reasonable within the distance range between Kiruna and regional stations (Assink et al., 2013).

The 2D transmission-loss maps at 1.5 Hz between source and receiver for the best atmospheric model, that is, the model leading to the largest regional infrasound amplitude, show that arrivals at IS37 (Figures 4a and 4b) and ARCI (Figures 4f and 4g) correspond to a combination of waves refracted at various altitudes. The back-scattering enabled by the inhomogeneities of GW, from around midway between source and a station, facilitates the ducting of the main arrivals at IS37 and occurs at lower (25–30 km) altitude than for ARCI (40–45 km), because IS37 closer than ARCI. The best atmospheric models give a good match between simulated and recorded time signal envelopes at both IS37 and ARCI (Figures 4c, 4d, 4h and 4i). Hernandez et al. (2018) suggested that regional infrasound data can provide constraints on Surface Pressure Level (SPL) around the epicenter for accurate TL

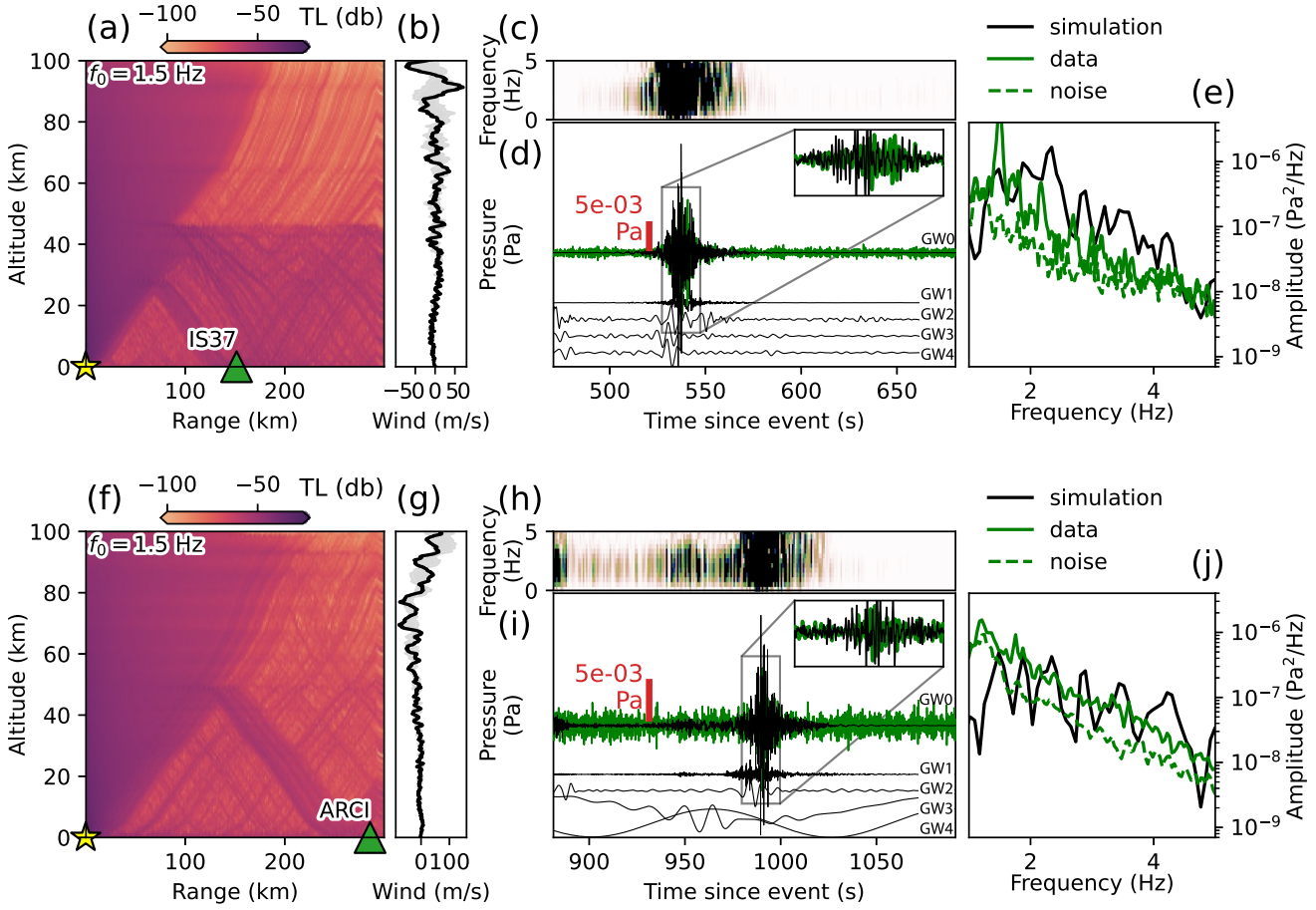

Figure 4. Regional infrasound data modeling at (a, b, c, d, e) IS37 and (f, g, h, i, j) ARCI (a), (f) Transmission loss versus range and altitude for the best atmospheric model along with (b), (g) along-track winds (black) and wind amplitudes for other gravity wave realizations (shaded gray) (c), (h) Spectrograms computed from the best-fitting numerical solutions (d), (i) Recorded (green) and simulated (black) signals for different gravity wave realizations. The amplitudes are scaled independently for each realization. Largest and smallest GW amplitudes for (d) $2.3e^{-2}$ and $5e^{-5}$ Pa and for (i) $1.5e^{-2}$ and $3.6e^{-12}$ Pa (e), (j) Power Spectral Density for recorded (orange), recorded noise (blue), and simulated signals (black). Waveforms are bandpass filtered between 0.5 and 5 Hz.

estimates. However, TL predictions with our best atmospheric model at 1.5 Hz yield an epicentral SPL, at 0.2 km from the source, of ~0.3 Pa using either ARCI or IS37 peak pressure readings. This clearly underestimates the SPL estimated at ~50 Pa using KRIS peak pressure, which can be due to the underprediction of infrasound energy above 2 Hz by our numerical model.

Note that the absence of GWs would produce a larger shadow zone without refraction down to regional stations. Meanwhile, other GW realizations lead to significantly lower amplitudes (bottom panels of Figures 4d and 4i) indicating a strong contribution of GW for arrivals to ARCI. The simulated spectral content for the best atmospheric models predicts an energy peak ~1.5 Hz at IS37 and ~1.8 Hz at ARCI, which is consistent with the observations (Figure 4e), but overpredicts the amplitude of frequency peaks at higher frequencies. This discrepancy highlights that our best atmospheric model is not a true description of the atmosphere. Infrasound multipathing is visible at ARCI with an early arrival at around 960 s which matches the observed arrival of coherent energy at about 960–970 s (Figure 1c).

Since (a) observed infrasound show a limited frequency range with high SNR, and (b) our simulations do not capture all the features of the recorded data using our best atmospheric model, we can not invert for source characteristics using regional data. However, we can still assess how much regional infrasound could inform a seismic source model in the ideal case of high SNR arrival through numerical simulations. We model high SNR signals using, as source-time functions, the waveforms simulated above the epicenter using a Gaussian source time function with half duration 1 s (energy <1.2 Hz). These source-time functions are averaged across three

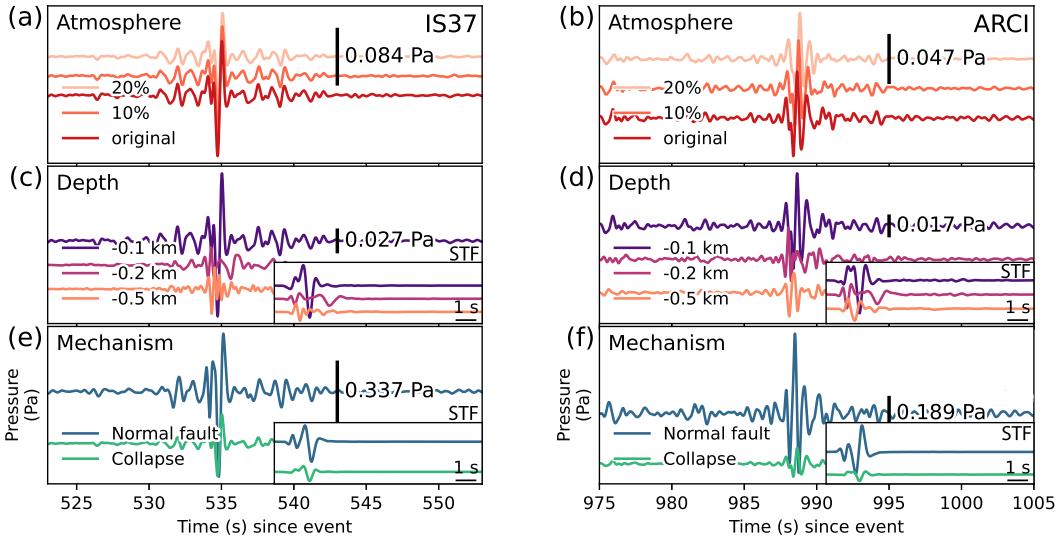

Figure 5. Atmospheric and source parameters effects on regional infrasound. Simulated waveforms for (a), (b) varying gravity wave amplitudes. The percentages correspond to a percentage of amplitude reduction compared to the original gravity wave realization (c), (d) varying focal depth (e), (f) varying source mechanism at IS37 (a, c, e), and ARCI (b, d, f). The Source-Time Functions (STF) are shown in the inset panels of (c, d, e, f).

different launch angles corresponding to waves refracting back to both IS37 (30–35° from vertical) and ARCI (40–45° from vertical).

While the phase of GWs have a significant impact on regional infrasound phase and amplitude, small amplitude variations of a given GW realization have an insignificant effect on the signal characteristics (Figures 5a and 5b). Focal depth and mechanism greatly influence the arrival time and main frequency peak of the local infrasound. Simulated regional signals are dominated by the negative of the original signals (Figures 5c–5e and 5f) which generally corresponds to waves traveling through second order caustics, that is, the intersection between slow arrival reflection caustic branches with the shadow zone caustic branches (Waxler et al., 2015). Comparing IS37 (Figures 5a–5c and 5e) and ARCI (Figures 5b–5d and 5f) we note that, in contrast to small variations of GW amplitudes, a larger-scale change ($\gg$5 km wavelength) in atmospheric winds severely impacts travel paths and the spectral content of the main infrasound arrivals.

6. Conclusions

The 2020 Kiruna minequake was the largest-ever recorded mining-induced seismic event in Sweden. For the first time ever, the epicentral infrasound signature of a shallow seismic event was detected at both local and regional distances. Local infrasound waves were accurately modeled up to 0.5 Hz while regional infrasound is challenging to reproduce due to both atmospheric path effects and their low SNRs. The independent inversion of regional seismic and local acoustic records both show clear signatures of a shallow collapse event at about 1 km depth in the northern section of the Kiruna mine. This solution is in agreement with the in-mine seismic records (Dineva et al., 2022). Discrepancies between simulated and observed signals are explained by various seismic-to-acoustic coupling effects exciting strong acoustic waves. This includes tunnel resonance, surface slip, and unconstrained shallow seismic velocities.

Regional simulations using realistic atmospheric models together with a realization of GW perturbations match well the observed signal envelopes at IS37 and ARCI despite discrepancies in terms of spectral content >2 Hz. This good fit benefited from the use of local records at KRIS which captures accurately the source effects. Our numerical sensitivity analysis highlighted a strong phase and amplitude dependence on focal depth and mechanism. Such strong dependence could allow us to map regional infrasound to specific source characteristics for future events when the infrasound path is known and for large-enough signal-to-noise ratios.

However, the quality of the source mechanism retrieval at regional scale depends on the atmospheric model accuracy used in the infrasound propagation modeling (Averbuch et al., 2022). Therefore, future research could

explore a wider range of possible atmospheric profiles using all ensemble members and a larger set of GW realizations to assess the uniqueness of the synthetic solutions. Importantly, it will be key to incorporate both acoustic and seismic data in the same inversion framework to fully exploit seismo-acoustic datasets. Nevertheless, the combination of full-waveform seismo-acoustic simulations in the near-field and normal-mode simulations in the far field can provide a practical framework to analyze seismically induced infrasound.

This study highlighted the potential and challenges associated with local and regional infrasound recordings to retrieve seismic source characteristics, which is particularly relevant in regions with poor seismic coverage (Shani-Kadmiel et al., 2021). Importantly, the good phase and amplitude fits between simulated and observed signals suggest that explosive sources can be discriminated from collapse events in pressure recordings, since the resulting explosive waveforms show an opposite sign compared to collapse waveforms. This can be particularly valuable when discriminating between nuclear explosions, earthquakes, and other seismic sources in remote regions. The detection of seismically induced infrasound and a better understanding of seismo-acoustic coupling mechanisms might also be key when exploring other planets' interiors, such as Venus (Brissaud et al., 2021; Garcia et al., 2022).

Conflict of Interest

The authors declare that they have no competing interests.

Data Availability Statement

Recorded and synthetic waveform data are available at Brissaud (2024a). Codes to invert local infrasound data and reproduce the Figures shown in the manuscript can be accessed here Brissaud (2024b). The seismic moment tensor inversion code "cut-and-paste" is available at Zhu and Helmberger (1996). The SPECFEM-DG code is available at Martire et al. (2022b). The ModBB normal mode code is available at Waxler et al. (2021). The code to produce gravity wave realizations is available at Brissaud et al. (2022). The emcee package can be downloaded here Foreman-Mackey et al. (2013b). The Kiruna minequake timing and location as well as seismic data were extracted from the Swedish National Seismic Network (SNSN) catalog available at Lund, Schmidt, Shomali, and Roth (2021).

Acknowledgments

Quentin Brissaud and Antoine Turquet are co-first authors. The authors thank Tormod Kvaerna and Marouchka Froment for valuable insight and advice during this work. The authors are grateful for constructive feedback and valuable suggestions from two anonymous reviewers. We also thank Björn Lund at the Swedish National Seismic Network for discussion and for providing origin times and hypocentral data for the Kiruna event. This work received support from the *Airborne Inversion of Rayleigh wave* (AIR) project, funded by the Research Council of Norway basic research program FRIPRO/FRINATEK, Contract 335903, and the *Middle Atmosphere Dynamics: Exploiting Infrasound Using a Multidisciplinary Approach at High Latitudes* (MADEIRA) project, funded by the Research Council of Norway basic research program FRIPRO/FRINATEK, Contract 274377, as well as NORSAR institute funding.

References

Alvizuri, C., Silwal, V., Krischer, L., & Tape, C. (2018). Estimation of full moment tensors, including uncertainties, for nuclear explosions, volcanic events, and earthquakes. *Journal of Geophysical Research: Solid Earth*, *123*(6), 5099–5119. https://doi.org/10.1029/2017JB015325

Arrowsmith, S. J., Burlacu, R., Pankow, K., Stump, B., Stead, R., Whitaker, R., & Hayward, C. (2012). A seismoacoustic study of the 2011 January 3 Circleville earthquake. *Geophysical Journal International*, *189*(2), 1148–1158. https://doi.org/10.1111/j.1365-246X.2012.05420.x

Assink, J., Waxler, R., Frazier, W., & Lonzaga, J. (2013). The estimation of upper atmospheric wind model updates from infrasound data. *Journal of Geophysical Research: Atmospheres*, *118*(19), 10–707. https://doi.org/10.1002/jgrd.50833

Averbuch, G., Ronac-Giannone, M., Arrowsmith, S., & Anderson, J. (2022). Evidence for short temporal atmospheric variations observed by infrasonic signals: 1. The troposphere. *Earth and Space Science*, *9*(3), e2021EA002036. https://doi.org/10.1029/2021EA002036

Averbuch, G., Waxler, R. M., Smets, P. S., & Evers, L. G. (2020). Probabilistic inversion for submerged source depth and strength from infrasound observations. *Journal of the Acoustical Society of America*, *147*(2), 1066–1077. https://doi.org/10.1121/10.0000695

Brissaud, Q. (2024a). Kiruna minequake seismo-acoustic dataset. [Dataset]. https://doi.org/10.6084/m9.figshare.25583364.v1. *figshare*.

Brissaud, Q. (2024b). Kiruna minequake seismo-acoustic codes. [Software]. https://github.com/QuentinBrissaud/Kiruna. *GitHub*.

Brissaud, Q., Krishnamoorthy, S., Jackson, J. M., Bowman, D. C., Komjathy, A., Cutts, J. A., et al. (2021). The first detection of an earthquake from a balloon using its acoustic signature. *Geophysical Research Letters*, *48*(12), e2021GL093013. https://doi.org/10.1029/2021GL093013

Brissaud, Q., Martin, R., Garcia, R. F., & Komatitsch, D. (2017). Hybrid Galerkin numerical modelling of elastodynamics and compressible Navier–Stokes couplings: Applications to seismo-gravito acoustic waves. *Geophysical Journal International*, *210*(2), 1047–1069. https://doi.org/10.1093/gji/ggx185

Brissaud, Q., Näsholm, S. P., & Turquet, A. (2022). A Python implementation of Gardner's model. [Software]. https://doi.org/10.6084/m9.figshare.19729738.v1. *figshare*.

Cansi, Y. (1995). An automatic seismic event processing for detection and location: The PMCC method. *Geophysical Research Letters*, *22*(9), 1021–1024. https://doi.org/10.1029/95gl00468

Chunchuzov, I., & Kulichkov, S. (2019). Internal gravity wave perturbations and their impacts on infrasound propagation in the atmosphere. In *Infrasound monitoring for atmospheric studies* (pp. 551–590). Springer. https://doi.org/10.1007/978-3-319-75140-5_16

Dannemann Dugick, F., Koch, C., Berg, E., Arrowsmith, S., & Albert, S. (2023). A new decade in seismoacoustics (2010–2022). *Bulletin of the Seismological Society of America*, *113*(4), 1390–1423. https://doi.org/10.1785/0120220157

Dineva, S., Dahnér, C., Malovichko, D., & Rudzinski, L. (2022). Analysis of the magnitude 4.2 seismic event on 18 may 2020 in the Kiirunvaara mine, Sweden. In *Proceedings of the tenth conference on rockburst and seismicity in mines*. Society for Mining, Metallurgy and Exploration.

Donn, W. L., & Posmentier, E. S. (1964). Ground-coupled air waves from the great Alaskan earthquake. *Journal of Geophysical Research*, *69*(24), 5357–5361. https://doi.org/10.1029/JZ069i024p05357

Downey, N., Albert, S., & Tibi, R. (2022). The Redmond salt mine monitoring experiment: Observations of infrasound resonance. *Bulletin of the Seismological Society of America*, *113*(4), 1664–1681. https://doi.org/10.1785/0120220114
Foreman-Mackey, D., Hogg, D. W., Lang, D., & Goodman, J. (2013a). emcee: The MCMC hammer. *Publications of the Astronomical Society of the Pacific*, *125*(925), 306–312. https://doi.org/10.1086/670067
Foreman-Mackey, D., Hogg, D. W., Lang, D., & Goodman, J. (2013b). emcee: The MCMC hammer. *Publications of the Astronomical Society of the Pacific*, *125*(925), 306–312. https://doi.org/10.1086/670067
Garcia, R. F., Klotz, A., Hertzog, A., Martin, R., Gérier, S., Kassarian, E., et al. (2022). Infrasound from large earthquakes recorded on a network of balloons in the stratosphere. *Geophysical Research Letters*, *49*(15), e2022GL098844. https://doi.org/10.1029/2022GL098844
Gardner, C. S., Hostetler, C. A., & Franke, S. J. (1993). Gravity wave models for the horizontal wave number spectra of atmospheric velocity and density fluctuations. *Journal of Geophysical Research*, *98*(D1), 1035–1049. https://doi.org/10.1029/92JD02051
Godin, O. A. (2011). Low-frequency sound transmission through a gas–solid interface. *Journal of the Acoustical Society of America*, *129*(2), EL45–EL51. https://doi.org/10.1121/1.3535578
Hejrani, B., Tkalcic, H., & Fichtner, A. (2017). Centroid moment tensor catalogue using a 3-D continental scale Earth model: Application to earthquakes in Papua New Guinea and the Solomon Islands. *Journal of Geophysical Research: Solid Earth*, *122*(7), 5517–5543. https://doi.org/10.1002/2017JB014230
Hernandez, B., Pichon, A. L., Vergoz, J., Herry, P., Ceranna, L., Pilger, C., et al. (2018). Estimating the ground-motion distribution of the 2016 Mw 6.2 Amatrice, Italy, earthquake using remote infrasound observations. *Seismological Research Letters*, *89*(6), 2227–2236. https://doi.org/10.1785/0220180103
Hersbach, H., Bell, B., Berrisford, P., Hirahara, S., Horányi, A., Muñoz-Sabater, J., et al. (2020). The ERA5 global reanalysis. *Quarterly Journal of the Royal Meteorological Society*, *146*(730), 1999–2049. https://doi.org/10.1002/qj.3803
Hersbach, H., Bell, B., Berrisford, P., Hirahara, S., Horányi, A., Muñoz-Sabater, J., et al. (2017). Complete ERA5 from 1940: Fifth generation of ECMWF atmospheric reanalyses of the global climate. https://doi.org/10.24381/cds.143582cf. accessed on 20 Jan 2024.
Hu, J., Pham, T.-S., & Tkalcic, H. (2023). Seismic moment tensor inversion with theory errors from 2-D Earth structure: Implications for the 2009–2017 DPRK nuclear blasts. *Geophysical Journal International*, *235*(3), 2035–2054. https://doi.org/10.1093/gji/ggad348
Inchin, P., Snively, J., Kaneko, Y., Zettergren, M., & Komjathy, A. (2021). Inferring the evolution of a large earthquake from its acoustic impacts on the ionosphere. *AGU Advances*, *2*(2), e2020AV000260. https://doi.org/10.1029/2020AV000260
Kim, K., & Pasyanos, M. E. (2022). Yield estimation of the august 2020 Beirut explosion by using physics-based propagation simulations of regional infrasound. *Geophysical Research Letters*, *49*(23), e2022GL101118. https://doi.org/10.1029/2022GL101118
Lai, V. H., Zhan, Z., Brissaud, Q., Sandanbata, O., & Miller, M. S. (2021). Inflation and asymmetric collapse at Kīlauea summit during the 2018 eruption from seismic and infrasound analyses. *Journal of Geophysical Research: Solid Earth*, *126*(10), e2021JB022139. https://doi.org/10.1029/2021JB022139
Laske, G., Masters, G., Ma, Z., & Pasyanos, M. (2013). Update on CRUST1.0 – a 1-degree global model of Earth's crust. *Geophysical Research Abstracts*, *15*, 2658. EGU General Assembly Vienna, Austria. https://doi.org/10.17611/DP/emccrust10
Le Pichon, A., Blanc, E., & Hauchecorne, A. (Eds.) (2010)., *Infrasound monitoring for atmospheric studies*. Springer.
Lund, B., Schmidt, P., Hossein Shomali, Z., & Roth, M. (2021). The modern Swedish national seismic network: Two decades of intraplate microseismic observation. *Seismological Research Letters*, *92*(3), 1747–1758. https://doi.org/10.1785/0220200435
Lund, B., Schmidt, P., Shomali, Z. H., & Roth, M. (2021b). SNSN: Swedish national seismic network. [Dataset]. *Uppsala University*. https://doi.org/10.18159/SNSN
Martire, L., Brissaud, Q., Lai, V. H., Garcia, R. F., Martin, R., Krishnamoorthy, S., et al. (2018). Numerical simulation of the atmospheric signature of artificial and natural seismic events. *Geophysical Research Letters*, *45*(21). https://doi.org/10.1029/2018GL080485
Martire, L., Martin, R., Brissaud, Q., & Garcia, R. F. (2022a). Specfem2d-dg, an open-source software modelling mechanical waves in coupled solid–fluid systems: The linearized Navier–Stokes approach. *Geophysical Journal International*, *228*(1), 664–697. https://doi.org/10.1093/gji/ggab308
Martire, L., Martin, R., Brissaud, Q., & Garcia, R. F. (2022b). Specfem2d-dg, an open-source software modelling mechanical waves in coupled solid–fluid systems: The linearized Navier–Stokes approach. [Software]. *GitHub*. https://doi.org/10.1093/gji/ggab308
Miksat, J., Müller, T., & Wenzel, F. (2008). Simulating three-dimensional seismograms in 2.5-dimensional structures by combining two-dimensional finite difference modelling and ray tracing. *Geophysical Journal International*, *174*(1), 309–315. https://doi.org/10.1111/j.1365-246x.2008.03800.x
Mutschlecner, J. P., & Whitaker, R. W. (2005). Infrasound from earthquakes. *Journal of Geophysical Research*, *110*(D1), D01–D108. https://doi.org/10.1029/2004JD005067
Pasyanos, M. E., Ichinose, G. E., & Ford, S. R. (2023). Moment tensor event identification for collapses. *Geophysical Journal International*, *235*(1), 635–643. https://doi.org/10.1093/gji/ggad258
Shani-Kadmiel, S., Assink, J. D., Smets, P. S. M., & Evers, L. G. (2018). Seismoacoustic coupled signals from earthquakes in central Italy: Epicentral and secondary sources of infrasound. *Geophysical Research Letters*, *45*(1), 427–435. https://doi.org/10.1002/2017GL076125
Shani-Kadmiel, S., Averbuch, G., Smets, P., Assink, J., & Evers, L. (2021). The 2010 Haiti earthquake revisited: An acoustic intensity map from remote atmospheric infrasound observations. *Earth and Planetary Science Letters*, *560*, 116795. https://doi.org/10.1016/j.epsl.2021.116795
Tape, W., & Tape, C. (2012). A geometric setting for moment tensors. *Geophysical Journal International*, *190*(1), 476–498. https://doi.org/10.1111/j.1365-246X.2012.05491.x
Vallage, A., Bollinger, L., Champenois, J., Duverger, C., Trilla, A. G., Hernandez, B., et al. (2021). Multitechnology characterization of an unusual surface rupturing intraplate earthquake: The ML 5.4 2019 Le Teil event in France. *Geophysical Journal International*, *226*(2), 803–813. https://doi.org/10.1093/gji/ggab136
Vorobeva, E., Assink, J., Espy, P. J., Renkwitz, T., Chunchuzov, I., & Näsholm, S. P. (2023). Probing gravity waves in the middle atmosphere using infrasound from explosions. *Journal of Geophysical Research: Atmospheres*, *128*(13), e2023JD038725. https://doi.org/10.1029/2023JD038725
Waxler, R., Evers, L. G., Assink, J., & Blom, P. (2015). The stratospheric arrival pair in infrasound propagation. *Journal of the Acoustical Society of America*, *137*(4), 1846–1856. https://doi.org/10.1121/1.4916718
Waxler, R., Hetzer, C., Assink, J., & Velea, D. (2021). NCPAprop v2.1.0. [Software]. *Zenodo*. https://doi.org/10.5281/zenodo.5562713
Yang, M., Wang, T., & Shi, J. (2021). Repeating infrasound from an earthquake doublet in Alaska. *Geophysical Research Letters*, *48*(17), e2021GL094632. https://doi.org/10.1029/2021GL094632
Zhu, L., & Helmberger, D. V. (1996). "cut-and-paste" seismic moment tensor inversion code. [Software]. https://github.com/uafgeotools/capuaf. *GitHub*.

Supporting Information for "Retrieving seismic source characteristics using seismic and infrasound data: The 2020 mb 4.9 Kiruna minequake, Sweden"

Antoine Turquet [1,*], Quentin Brissaud [1,*], Sven Peter Näsholm [1,2], Johan Kero [3], and Alexis Le Pichon [4]

[1]NORSAR, Gunnar Randers vei 15, Kjeller, Norway
[2]Department of Informatics, University of Oslo, P.O. Box 1080, NO–0316 Oslo, Norway
[3]Swedish Institute of Space Physics (IRF), Kiruna, Sweden
[4]CEA, DAM, DIF, F-91297 Arpajon, France

[*]These authors contributed equally to this work.

Contents of this file

S1 Introduction

This supporting information contains the six sections S1 to S7. These provide information on the atmospheric model setup (S1) and a description of the Transmission loss (TL) inversion methodology (S2). Figure S1 displays the estimated TL. Section S3 describes how we corrected for geometrical spreading. Section S4 discusses the full-waveform inversion of local infrasound data, as detailed in Figure S2. In Section S5, we discuss the impact of topography, source location, and subsurface properties on near-field infrasound Figures S4 and S5 and Table S1 are presented in this section. Section S6 discusses the seismic velocity model used and provides data in Tables S2 and S3. Finally, we provide details about the moment-tensor inversion of Section S7. We compare the recorded and synthetic waveforms in Figure S6 and provide a distribution of moment tensor solutions in Figure S7.

S2 Atmospheric model construction

Similar to the approach of Brissaud et al. (2023), atmospheric models are built as a combination of ERA-5 reanalysis models up to 80 km altitude together with the MSIS and HWM14 models for upper background atmospheric conditions and winds up to 120 km altitude. In order to account for unresolved wind perturbations in the stratosphere, we construct gravity-wave perturbations using Gardner's model.
Gardner's model characterizes the horizontal wave number spectra of wind perturbations assuming that both saturated and unsaturated waves obey the polarization and dispersion relations, and that the vertical wave number and temporal frequency are separable. The implemented horizontal wave number spectrum allows for calculating the horizontal correlation lengths of the wind perturbations. Random realizations of range-dependent perturbation terms are obtained and superimposed on the effective sound speed profiles in the propagation plane.

S3 Transmission-loss inversion methodology

Observed infrasound backazimuth data can directly provide constraints on the level of acoustic energy close to the epicenter which is a proxy for ground shaking (Hernandez et al., 2018). We backproject coherent local infrasound along the estimated backazimuth and a great

circle path to estimate the transmission loss around the source. This assumes a simple linear propagation path along the surface up to the KRIS array which is valid at local distance, in the absence of high topography (Averbuch et al., 2022), and especially at low frequencies (Supporting Information Sec. S6).

For the inversion, we used the following parameters for the minequake: origin time at 01:11:56.2 UTC with an error of ±0.1 s, sound velocity $c_s = 330 \pm 8$ m/s, and a backazimuth error of $e_{\text{baz}} = \pm 5$ degrees. The epicenter is located at (67.83965°N, 20.20759°E) and the station KRIS is located at (67.8549°N, 20.4220°E). To incorporate the possible error in backazimuth and origin time, we have perturbed our input parameters with a uniform distribution with 10 realizations and for the errors in backpropagation velocity, we have sampled a normal distribution with 15 realizations.

The amplitudes and backazimuths are obtained from PMCC analysis (i.e., pixels in PMCC) of station KRIS between 01:12:15 – 01:12:50 UTC. To correct for the propagation in the solid Earth, we have used

$$\Delta d = \sqrt{\frac{-h}{1-(v_s/v_a)^2}}, \tag{S1}$$

where Δd is the distance correction for the propagation time in the solid Earth, h is the focal depth, v_s is the seismic velocity, v_a is the acoustic velocity. The corrected propagating distances were used to correct the amplitudes for spherical spreading and converted to transmission loss using the formula $TL = 20log_{10}(A/A_r)$ where A is the distance corrected amplitude, A_r is the reference amplitude (1 Pa). Computed TL over multiple distances and probabilities were grouped over the predefined mesh and sorted according to their probabilities in each grid. The TL with the highest probability is chosen and plotted on the map.

The maximum SPL location fits the moment tensor solutions in the northern section of the mine (Fig. S1 but large TLs also spread along the propagation, most likely highlighting a temporal distribution of acoustic source sub-events.

S4 Geometrical spreading correction

Waveforms are simulated in 2D using SPECFEM-DG and therefore require a phase and amplitude correction due to 3D geometrical spreading effects. We adopt a simple procedure described in Miksat et al. (2008) that consists of convolving 2D waveforms with a time- and velocity-dependent correction. This formulation relies on the assumptions that the media are homogeneous and that the sources, for both acoustic and seismic waves, are point sources in space.

In a homogeneous acoustic medium, the ratio of 3D-to-2D Green's functions (equivalent to a 3D-to-2D ratio of fundamental-mode Rayleigh waves) gives us the correction factor C in the frequency domain (see Eq. (13) in Miksat et al. (2008)),

$$C(w) = \sqrt{\frac{|w|}{2\pi c r}} e^{-i\pi\,\text{sign}(w)/4}, \tag{S2}$$

where $w = 2\pi f$, where f (Hz) is the frequency, c (m/s) is the medium velocity, and r (m) is the source-receiver distance. We can then compute the 3D corrected waveform as,

$$s_{3\text{D}}(t,r) = \mathbb{F}^{-1}(C(w)\mathbb{F}(s_{2\text{D}}(t,r))), \tag{S3}$$

where $s_{2\text{D}}$ (Pa) is the waveform from 2D simulations, $\mathbb{F}$ is the Fourier transform, and $s_{3\text{D}}$ (Pa) is the 3D-corrected waveform.

Because this procedure depends on the medium velocity, we perform the scaling of seismic waves and acoustic waves independently by assuming a seismic wave velocity of $c_s = 3.5$ km/s, and an acoustic wave velocity of $c_a = 0.34$ km/s. The seismic velocity is taken as an upper bound of the Rayleigh wave velocity in the frequency range of interest, since Rayleigh waves dominate the recordings at KRIS. Although the surface wave velocity is frequency dependent, the small variations in seismic velocities (±0.5 km/s) in the scaling procedure as described in Eq. S2 and S3, impact the phase amplitude by less than 10%.

S5 Full-waveform inversion of local infrasound data

We perform a full-waveform inversion of local infrasound data by varying 7 inputs parameters: perturbation in origin time ϵ_{t_0} (s), perturbation in distance from the source ϵ_{dist} (km), perturbation in acoustic velocity $\epsilon_{c_{IS}}$ (km/s), 2D moment tensor components M_{xx}, M_{xz}, M_{zz}, and focal depth z_s (km). Assuming Gaussian-distributed noise, we can build the posterior probability $\mathbb{P}(\mathbf{m}|\mathbf{d}^{obs})$ for the 7 model parameters listed above $\mathbf{m}$ given the observation $\mathbf{d}^{obs}$ as (Hejrani et al., 2017)

$$\mathbb{P}(\mathbf{m}|\mathbf{d}^{obs}) = \frac{\mathbb{P}(\mathbf{m})}{(2\pi)^N |\mathbf{C}_k|^{1/2}} \exp\left[-\frac{1}{2}(\mathbf{d}^{obs}-\mathbf{d})^T \mathbf{C}_k^{-1}(\mathbf{d}^{obs}-\mathbf{d})\right],$$

where $\mathbb{P}(\mathbf{m})$ is the prior distribution of model parameters, $\mathbf{C}_k$ is the noise covariance matrix, and $\mathbf{d}$ is the synthetic waveform vector of size N. We consider here that the noise in our model originates only from the noise in the data, which can be described as $\mathbf{C}_k = w_t \sigma_n \mathbf{I}_d$, where $\sigma_n = 0.1$ (Pa) is the noise variance, $\mathbf{I}_d$ the identity matrix, and w_t is a weight over each sample in the waveform. To ensure that both seismic and acoustic arrivals, which

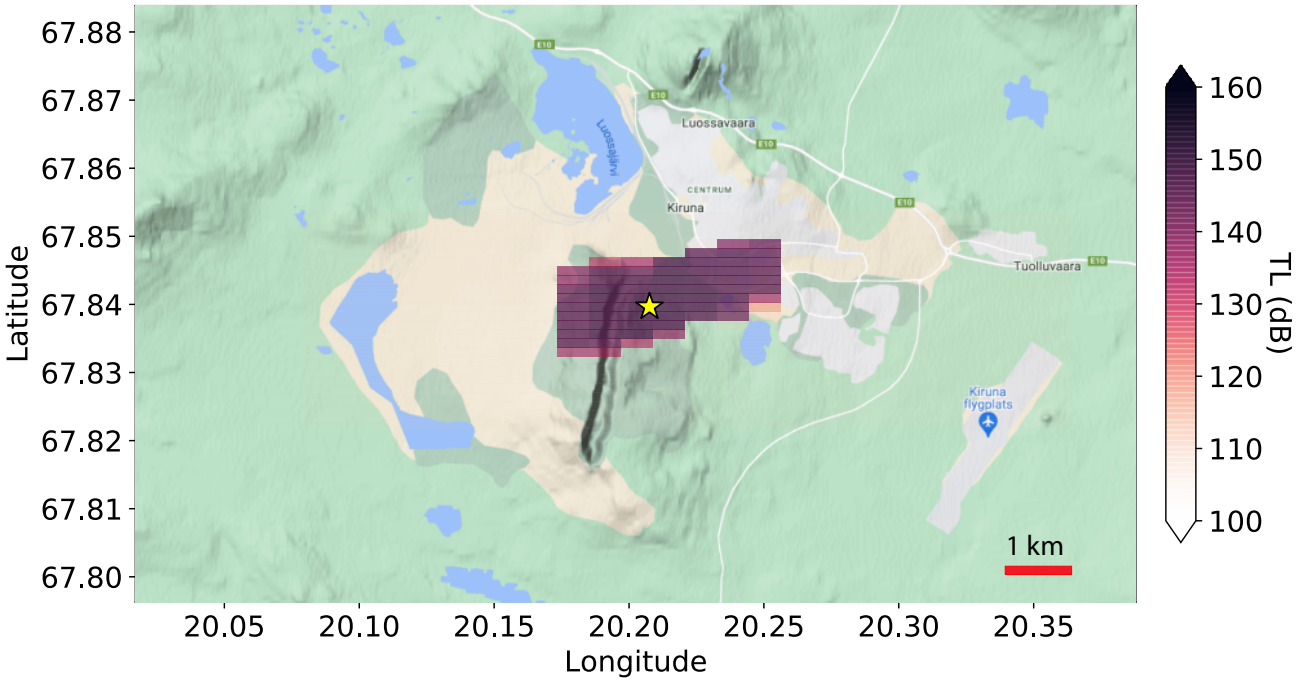

Figure S1. Back-projected Transmission Loss (TL in dB, with a normalization factor of 1 Pa) using KRIS data. The star corresponds to the epicenter.

have different amplitudes, contribute equally to the misfit, we weigh the misfit of acoustic arrival more by a factor 2.5 so that $w_{t<20s} = 1$ and $w_{t>20s} = 2.5$, where t is the time in seconds since the event. We consider Gaussian distributions $\mathcal{G}(\mu, \sigma)$, with μ, σ the mean and standard deviations of prior probabilities, so that $\mathbb{P}(\epsilon_{t_0}) = \mathcal{G}(0, 0.2)$, $\mathbb{P}(\epsilon_{c_{IS}}) = \mathcal{G}(0, 0.08)$, and $\mathbb{P}(\epsilon_{\text{dist}}) = \mathcal{G}(0, 2.)$. Finally, we sample the parameter space using a Markov chain Monte Carlo (MCMC) strategy with stretch moves and implemented in the *emcee* Python package (Foreman-Mackey et al., 2013).

We pre-computed the waveform catalog using SPECFEM-DG where we varied focal depth between 0.25 to 2 km with a 0.25 km step, and for 3 fundamental mechanisms $(M_{xx} = 1, M_{xz} = 0, M_{zz} = 0), (M_{xx} = 0, M_{xz} = 1, M_{zz} = 0), (M_{xx} = 0, M_{xz} = 0, M_{zz} = 1)$. This moment tensor decomposition approach is similar to the seismic full-waveform inversion approach of Hejrani et al. (2017). Variations in acoustic velocity and distance from the source require the running of new simulation results for each set of input parameters. However, at local distance, we can assume that the waves travel mostly linearly along the surface at constant velocity. Moreover, neither their phase nor their amplitude changes significantly over such short distances. Therefore, instead of recomputing a full-waveform solution with SPECFEM-DG, we simply shift in time between seismic and acoustic phases independently based on the origin time and distance from the source and for a given acoustic velocity. This time-shifting approach has been used to invert for underground explosion focal mechanism properties at the regional scale (Hu et al., 2023).

We observe a bi-modal structure in the focal depth MCMC sample distribution (Fig. S2). This can be explained by the fact that deep sources lead to better seismic predictions, i.e., a lower seismic-to-acoustic misfit (Fig. S3), while shallower sources lead to better acoustic predictions, i.e., a larger seismic-to-acoustic misfit.

S6 Impact of topography, source location, and subsurface properties on near-field infrasound signals

Various frequency-dependent contributions along the seismo-acoustic propagation path can affect the infrasound waveforms (Brissaud et al., 2021): Topography through wave scattering, subsurface seismic velocities that affect the coupling efficiency, and focal depth and epicenter. In order to assess their influence in the case of the Kiruna minequake, we considered various scenarios: (1) low- and high- frequency simulations without topography to investigate the impact of topography versus frequency, (2) a low-frequency simulation with a source south of the mine which differs from the dominating

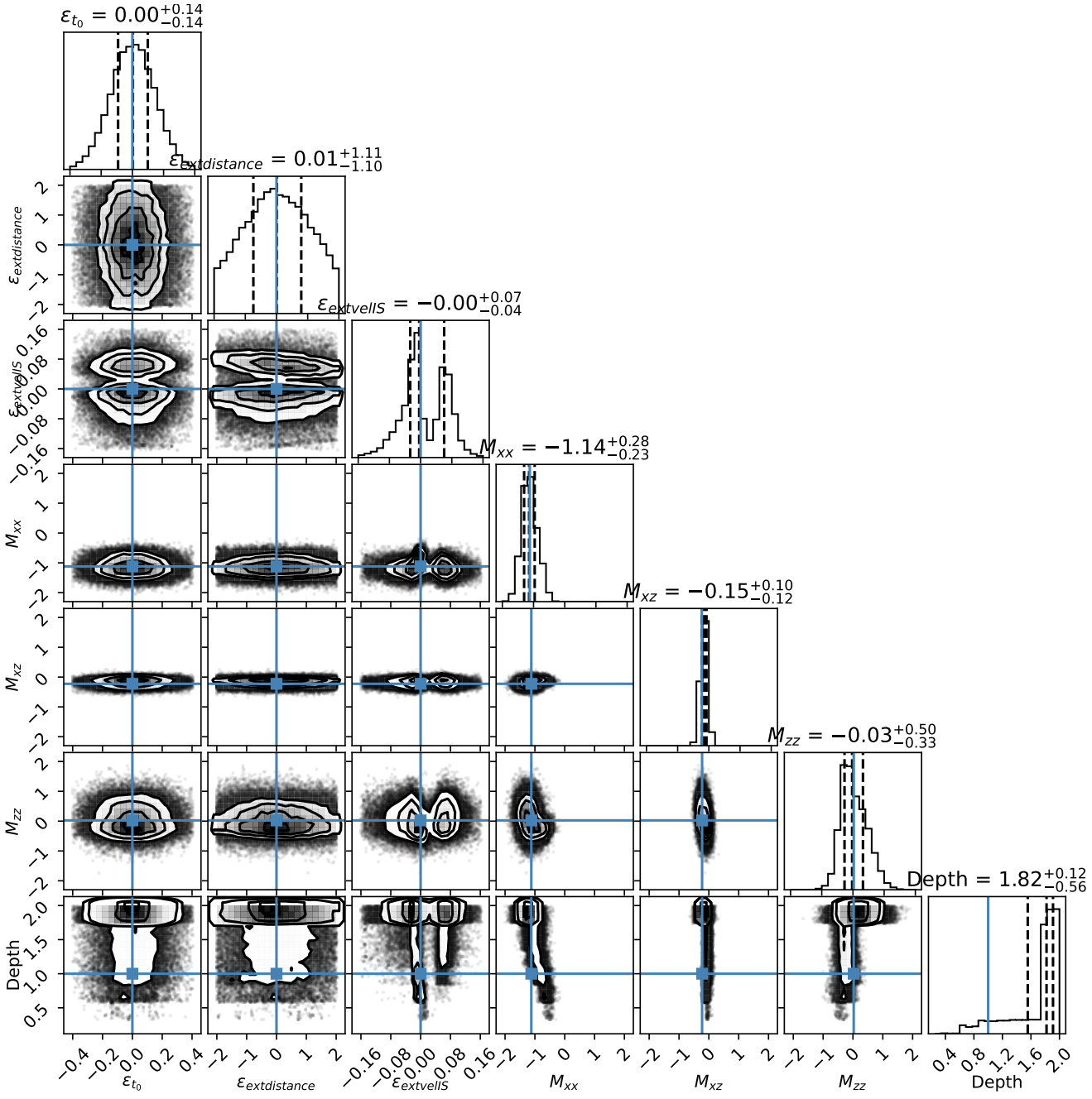

Figure S2. Distribution of MCMC samples for all inputs parameters perturbation in origin time ϵ_{t_0} (s), perturbation in distance from the source ϵ_{dist} (km), perturbation in acoustic velocity $\epsilon_{c_{IS}}$ (km/s), 2D moment tensor components M_{xx}, M_{xz}, M_{zz}, and focal depth z_s (km).

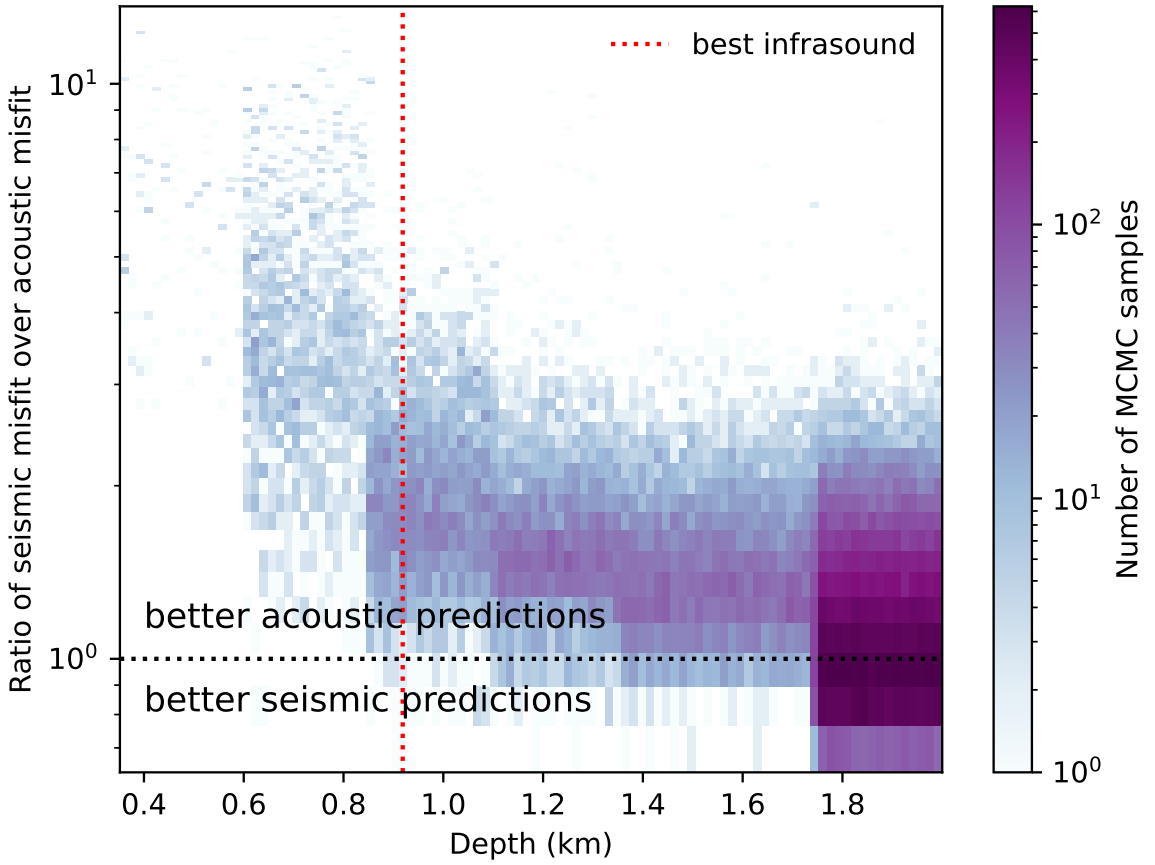

Figure S3. Ratio of seismic over acoustic misfit for all MCMC samples. Increasing values correspond to more accurate acoustic predictions and worse seismic predictions. On the contrary, decreasing values correspond to worse acoustic predictions and better seismic predictions.

collapse event epicenter, and (3) a high-frequency simulation with a sedimentary layer to showcase the impact of unconsolidated material on wave transmission. Simulation parameters are shown in Table S1 and seismic velocity models are described in Supporting Information Sec. S7.

Owing to the smoothness of the local topography, it has an insignificant impact on both the amplitude and phase of low-frequency signals (Fig. S4) but impacts the later seismic and acoustic arrivals at higher frequencies (Fig. S5). The epicenter location mostly delays the arrival of both seismic and acoustic waves by increasing the travel time (Fig. S4) since the collapse source is dominated by its isotropic component. At high frequencies, focal depth significantly impacts the amplitude of both seismic and acoustic arrivals, with shallower sources transmitting more energy to the atmosphere (Fig. S5). A sedimentary layer drastically increases the amplitude of both seismic and acoustic waves by exciting trapped waves in the shallow sedimentary layer.

S7 Seismic velocity model

The 1D seismic velocity model used for moment-tensor inversion and seismo-acoustic full-waveform simulations is described in Table S2. The 1D model with a sedimentary layer used in Section S6 is described in Table S3.

S8 Details about the moment-tensor inversion

In this Section, we provide more details about the best moment tensor solution described in Sec. 2 in the main text. Figure S6 shows all waveform fits for our best moment-tensor solution. A summary of the distribution

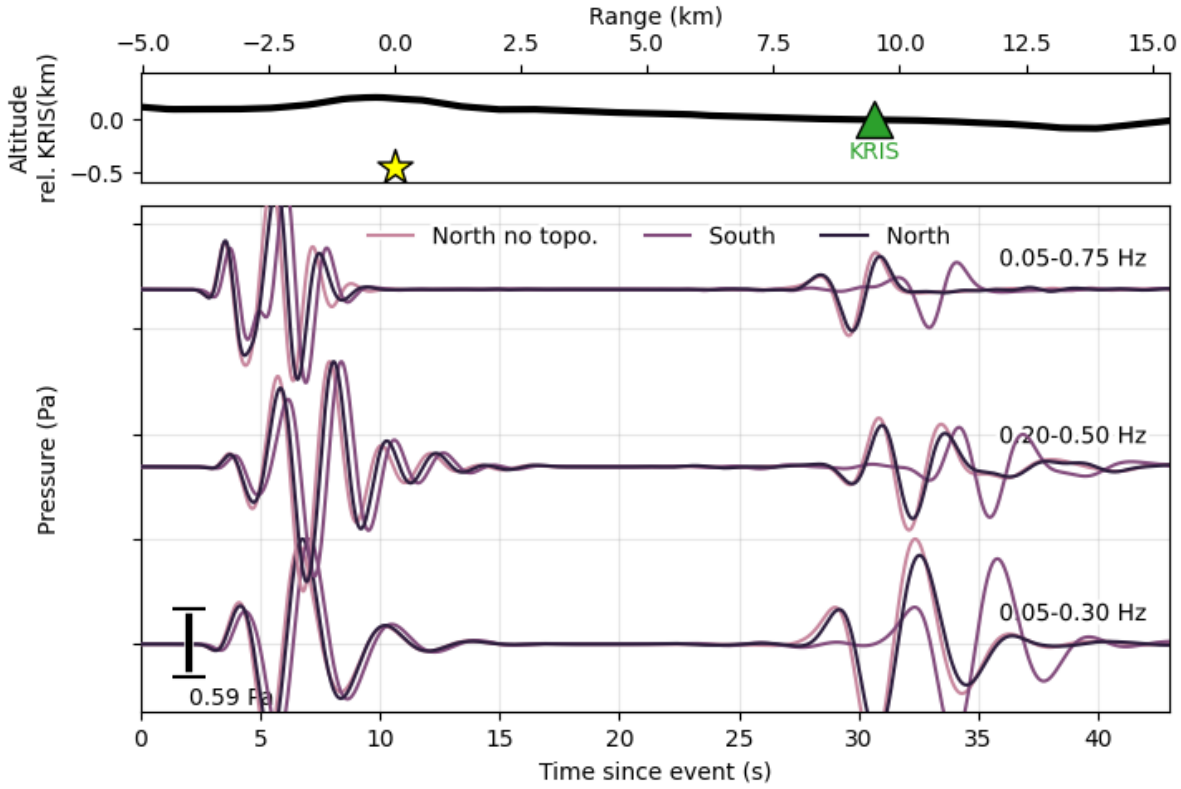

Figure S4. Simulated acoustic waveforms at KRIS for a low-frequency source at focal depth 0.5 km located north of the mine with topography (black) and without (light pink), and for a source located south of the mine (purple). Simulations parameters can be found in Table S1.

Table S1. Simulation parameters used for the sensitivity analysis in Supporting Information Sec. S6. North source location refers to latitude and longitude (67.8397°N, 20.2076°E). South source location refers to latitude and longitude (67.8251°N, 20.1891°E). The source time function is a Gaussian function. The moment tensor model corresponds the solution presented in the moment tensor analysis in the main text.

Source location	Corner frequency (Hz)	Focal depth (km)	Topography	Sediments	Reference
North	0.75	0.5	No	No	light pink, Fig. S5
North	0.75	0.5	Yes	No	black, Fig. S4
South	0.75	0.5	Yes	No	purple, Fig. S4
South	1.75	0.5	Yes	No	dark blue, Fig. S4
North	1.75	0.5	No	No	dark green, Fig. S5
North	1.75	0.5	Yes	Yes	green, Fig. S5
North	1.75	0.1	Yes	No	red, Fig. S5

Table S2. 1D seismic velocity derived from CRUST1.0. V_s (km/s) is the shear velocity. V_p (km/s) is the compressional velocity. ρ is the density. Q_s and Q_p are the shear- and compressional-wave quality factors.

Thickness (km)	V_s (km/s)	V_p (km/s)	ρ (kg/m^3)	Q_s	Q_s
0.01	0.55	2.00	1.93	500	1000
1.96	2.70	5.00	2.55	500	1000
3.94	3.70	6.50	2.85	500	1000
13.76	4.05	7.10	3.05	500	1000
1000	4.28	7.68	3.17	500	1000

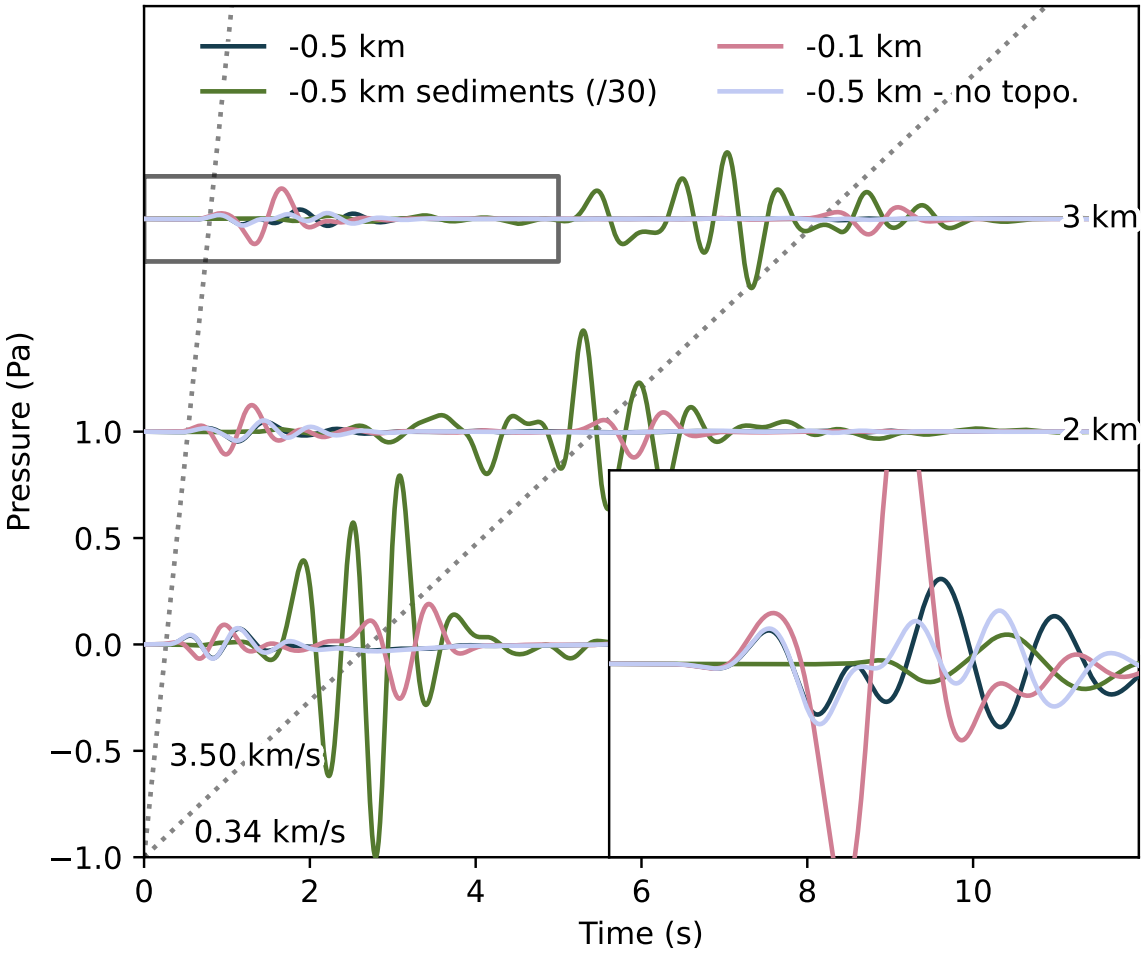

Figure S5. Simulated acoustic waveforms at KRIS for a high-frequency source at focal depth 0.5 km (dark blue, green, light purple) or 0.1 km (light red), without topography (light purple), and with a sedimentary layer (amplitude divided by 40, green). Simulation parameters can be found in Table S1.

Table S3. 1D seismic velocity derived from CRUST1.0 with sedimentary layer. V_s (km/s) is the shear velocity. V_p (km/s) is the compressional velocity. ρ is the density. Q_s and Q_p are the shear- and compressional-wave quality factors.

Thickness (km)	V_s (km/s)	V_p (km/s)	ρ (kg/m^3)	Q_s	Q_s
0.25	0.55	2.00	1.93	500	1000
1.96	2.70	5.00	2.55	500	1000
3.94	3.70	6.50	2.85	500	1000
13.76	4.05	7.10	3.05	500	1000
1000	4.28	7.68	3.17	500	1000

of moment tensor solutions and the corresponding accuracies when reproducing the observed waveforms is shown in Fig. S7.

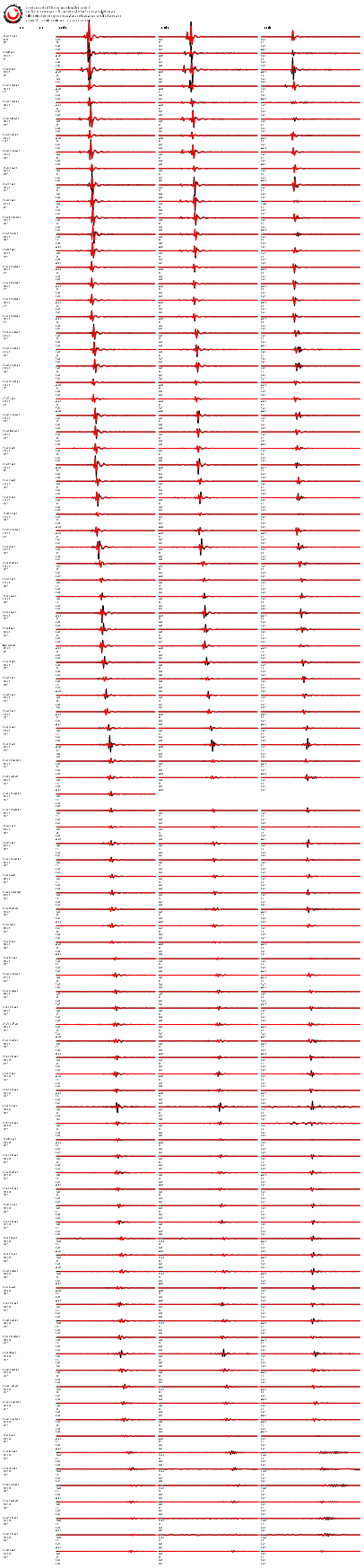

Figure S6. Comparison between recorded (black) and synthetic (red) seismic waveforms for all the 93 stations used for inversion. The image file can be downloaded separately.

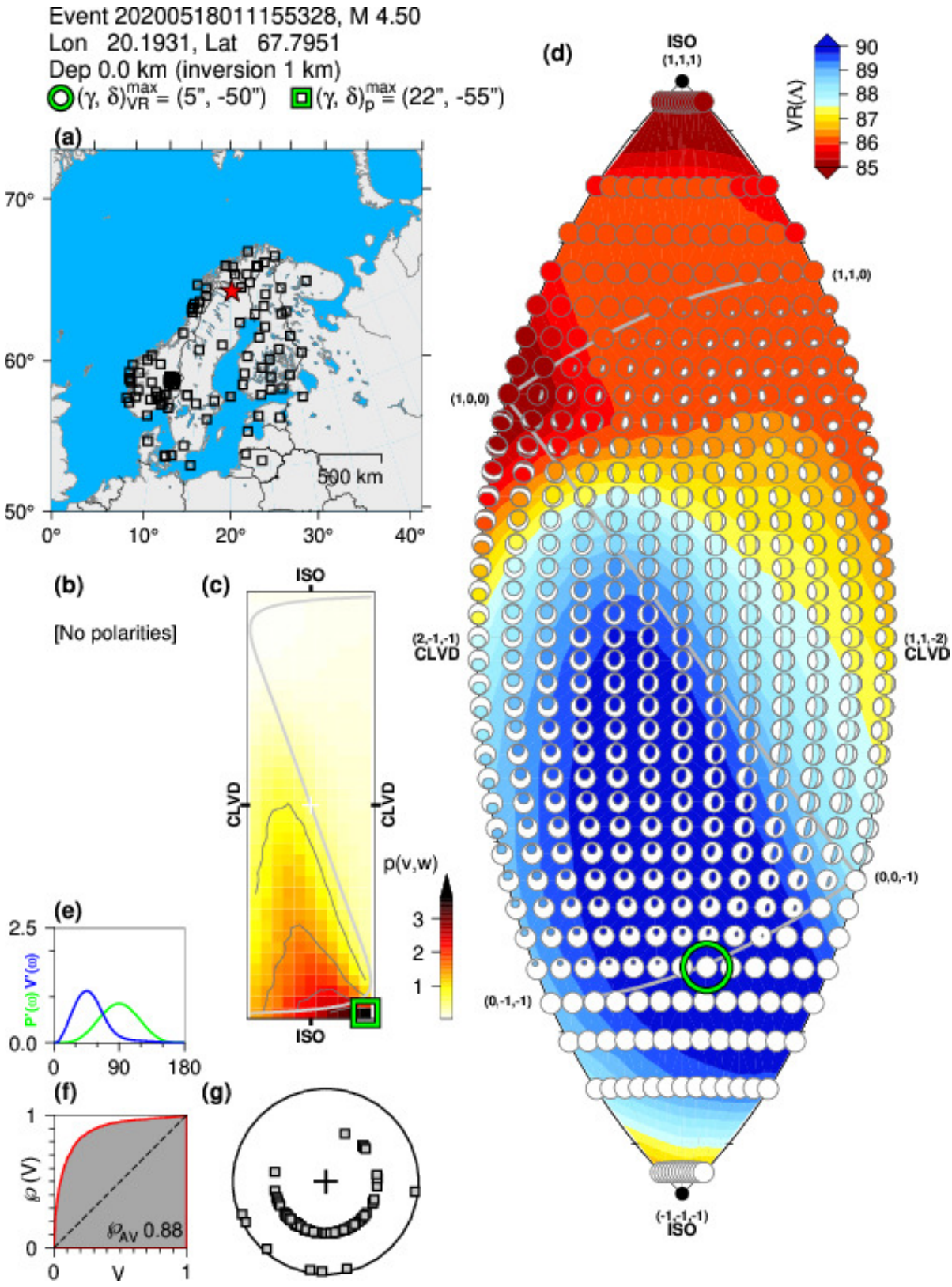

Figure S7. Full grid search summary on a lune diagram, showing the best-fitting solution at each grid point on the lune and colored by waveform fit, with best-fitting solutions in blue and worst-fitting solutions in red.

References

G. Averbuch, M. Ronac-Giannone, S. Arrowsmith, and J. Anderson. Evidence for short temporal atmospheric variations observed by infrasonic signals: 1. The troposphere. *Earth and Space Science*, 9(3):e2021EA002036, 2022. https://doi.org/10.1029/2021EA002036.

Q. Brissaud, S. Krishnamoorthy, J. M. Jackson, D. C. Bowman, A. Komjathy, J. A. Cutts, Z. Zhan, M. T. Pauken, J. S. Izraelevitz, and G. J. Walsh. The first detection of an earthquake from a balloon using its acoustic signature. *Geophysical Research Letters*, 48(12):e2021GL093013, 2021. https://doi.org/10.1029/2021GL093013.

Q. Brissaud, S. P. Näsholm, A. Turquet, and A. Le Pichon. Predicting infrasound transmission loss using deep learning. *Geophysical Journal International*, 232(1):274–286, 2023.

D. Foreman-Mackey, D. W. Hogg, D. Lang, and J. Goodman. emcee: The MCMC hammer. *Publications of the Astronomical Society of the Pacific*, 125(925):306–312, feb 2013. https://doi.org/10.1086/670067.

B. Hejrani, H. Tkalcic, and A. Fichtner. Centroid moment tensor catalogue using a 3-D continental scale Earth model: Application to earthquakes in Papua New Guinea and the Solomon Islands. *Journal of Geophysical Research: Solid Earth*, 122(7):5517–5543, 2017. https://doi.org/10.1002/2017JB014230.

B. Hernandez, A. L. Pichon, J. Vergoz, P. Herry, L. Ceranna, C. Pilger, E. Marchetti, M. Ripepe, and R. Bossu. Estimating the ground-motion distribution of the 2016 Mw 6.2 Amatrice, Italy, earthquake using remote infrasound observations. *Seismological Research Letters*, 89(6):2227–2236, Nov. 2018. ISSN 0895-0695. https://doi.org/10.1785/0220180103.

J. Hu, T.-S. Pham, and H. Tkalcic. Seismic moment tensor inversion with theory errors from 2-D Earth structure: implications for the 2009–2017 DPRK nuclear blasts. *Geophysical Journal International*, 235(3):2035–2054, 2023. https://doi.org/10.1093/gji/ggad348.

J. Miksat, T. Müller, and F. Wenzel. Simulating three-dimensional seismograms in 2.5-dimensional structures by combining two-dimensional finite difference modelling and ray tracing. *Geophysical Journal International*, 174(1): 309–315, 2008.